PHYSICAL REVIEW B **108**, 054303 (2023)

Quantifying the lattice and electronic thermal conductivity of arsenic from first principles

Guijian Pang[1,*] Bo Zhang,[1,*] Fanchen Meng,[2,3] Zhe Liu,[1] Yani Chen,[1,†] and Wu Li[1,‡]
[1]*Institute for Advanced Study, Shenzhen University, Shenzhen 518060, China*
[2]*Center for Functional Nanomaterials, Brookhaven National Laboratory, Upton, New York 11973, USA*
[3]*Research Computing and Data, Clemson Computing and Information Technology, Clemson University, Clemson, South Carolina 29634, USA*

(Received 4 March 2023; revised 18 July 2023; accepted 25 July 2023; published 10 August 2023; corrected 26 February 2025)

We have calculated the lattice and electronic thermal conductivity of arsenic between 50 and 500 K by using the first-principles Boltzmann transport equation. We find that the lattice thermal conductivity (κ_{ph}) exhibits strong anisotropy: the calculated room-temperature κ_{ph} is 18.6 and 5.8 W m^{-1} K^{-1} along the binary and trigonal directions, respectively. The anisotropy of κ_{ph} is mainly ascribed to the longitudinal acoustic phonon branch. κ_{ph} in the binary direction is larger than those reported for most of the other elemental metals. The electronic thermal conductivity (κ_{e}) is almost isotropic, and almost independent of temperature above 150 K, with a room-temperature value of ~26 W m^{-1} K^{-1}. κ_{e} dominates over κ_{ph} in the binary direction above 200 K. Compared to the neighboring element Ge, As has comparable harmonic but much stronger anharmonic interatomic interactions. These strong anharmonic interactions in As are the dominant mechanism limiting κ_{ph}. Despite a larger carrier concentration in As than in Bi or Sb, the phonon-electron interactions hardly affect κ_{ph} at room temperature. The calculated total thermal conductivity is in good agreement with the experimental values. Our work provides more insights into the thermal transport in elemental semimetals.

DOI: 10.1103/PhysRevB.108.054303

I. INTRODUCTION

Thermal transport in metals and nonmetals is fundamentally different. Phonons dominate the thermal conductivity in nonmetals, whereas they contribute negligibly to the thermal conductivity both relatively and absolutely in metals, with limited exceptions, at all temperatures [1,2]. In metals, at low temperatures in particular, phonon-electron scattering limits the lattice thermal conductivity, thus κ_{ph} follows a T^2 temperature dependence. Consequently, κ_{ph} is usually much smaller than the electronic contribution κ_{e}, which follows a linear T dependence arising from defect scattering [3,4].

κ_{ph} displays different characteristics in semimetals. Due to a reduced number of free carriers, the lattice contribution can dominate the thermal conduction at low temperatures, and thus κ_{ph} can be easily measured even without separating out κ_{e} [5]. This is what happens in the group-V elemental crystals, Sb and Bi. The measured total κ indeed shows a T^2 dependence in Sb [6]. However, κ in Bi is mostly limited by the boundary rather than the phonon-electron scattering, due to the lower carrier density [7].

In arsenic, another group-V semimetal but with higher carrier density, κ_{ph} remains much smaller than κ_{e} at low temperatures. Interestingly, it had been found experimentally that κ_{ph} becomes predominant over κ_{e} along the binary direction above 15 K [8]. Furthermore, strong anisotropy was demonstrated for κ_{ph} measured up to 100 K, in contrast to the nearly isotropic κ_{ph} in Bi and Sb. Experimentally, κ_{ph} can be measured by applying a magnetic field to suppress κ_{e}. However, due to the limit of a magnetic field, previous measurements separated κ_{ph} and κ_{e} directly only up to 37 K for As [8]. As for higher temperatures, the separation was further estimated by using an extrapolation method. In addition, Heremans *et al.* separated κ_{ph} and κ_{e} following the Wiedemann-Franz law (WFL) with parametrized Lorenz numbers [9]. However, the validity of the WFL to estimate κ_{e} from the electronic conductivity is not always guaranteed for quantitative analysis. Reliable knowledge of κ_{ph} of As around the ambient temperature is still lacking.

In this paper, we have quantified the electronic and lattice contributions to the total thermal conductivity in As by solving the phonon and electron Boltzmann transport equation (BTE) from first principles. The predicted κ_{ph} is highly anisotropic, which is mainly attributed to the longitudinal acoustic (LA) phonon modes. κ_{ph} along the binary direction is found to be larger than those reported for most other elemental metals, and it becomes predominant over κ_{e} below 200 K. On the other hand, the κ_{e} is isotropic and nearly independent of temperatures between 150 and 500 K. The total thermal conductivity (κ_{t}) obtained in this work is in good agreement with the experimental results.

II. METHODOLOGY

A. Phonon BTE and lattice thermal conductivity

The Boltzmann transport equation can describe phonon and electron transport behaviors at the mode-specific level. Within the framework of a linearized phonon BTE, the lattice

---

[*] These authors contributed equally to this work.
[†] chenyn@szu.edu.cn
[‡] wu.li.phys2011@gmail.com

thermal conductivity tensor κ_{ph} can be calculated using the expression [10]

$$\kappa_{\mathrm{ph}} = \frac{1}{N_{\mathbf{q}} V k_B T^2} \sum_{\lambda} n_{\lambda}^{0} \left(n_{\lambda}^{0} + 1 \right) (\hbar \omega_{\lambda})^2 \mathbf{v}_{\lambda} \otimes \mathbf{F}_{\lambda}. \tag{1}$$

Here, V is the unit-cell volume and $N_{\mathbf{q}}$ is the total number of $\mathbf{q}$ points to uniformly sample in the Brillouin zone. n_{λ}^{0}, ω_{λ}, and $\mathbf{v}_{\lambda}$ are the equilibrium Bose-Einstein distribution, angular frequency, and group velocity, respectively, for specific phonon mode λ, which comprises a certain branch index p and wave vector $\mathbf{q}$. $\mathbf{F}_{\lambda}$ is the phonon mean free displacement. Thereby, the compact form of the linearized phonon BTE can be expressed as

$$\mathbf{F}_{\lambda} = \tau_{\lambda} (\mathbf{v}_{\lambda} + \mathbf{\Delta}_{\lambda}), \tag{2}$$

where τ_{λ} is the total phonon relaxation time, the inverse of which denotes the total scattering rate accounting for all specific phonon scattering mechanisms for any given system. In this study, the naturally occurring As, as well as Sb and Bi, are nearly isotopically pure, leading to a negligible phonon-isotope scattering. Therefore, only anharmonic phonon-phonon and phonon-electron scattering dominates the scattering processes, which can be treated as [11]

$$\frac{1}{\tau_{\lambda}} = \frac{1}{\tau_{\lambda}^{\text{ph-ph}}} + \frac{1}{\tau_{\lambda}^{\text{ph-el}}}. \tag{3}$$

Note that anharmonic scattering is governed by three-phonon processes. The $\mathbf{\Delta}_{\lambda}$ term is a linear combination of $\mathbf{F}_{\lambda}$, indicating that Eq. (2) is a set of linear equations. Hence, the $\mathbf{F}_{\lambda}$ can be solved accurately using the iterative approach (see Supplemental Material) [12].

B. Electron BTE and electronic thermal conductivity

Within the electron BTE, the electronic conductivity tensor (σ) at a given temperature T can be written as [13–15]

$$\sigma = \frac{2e^2}{N_{\mathbf{k}} V k_B T} \sum_{n\mathbf{k}} f_{n\mathbf{k}}^{0} \left(1 - f_{n\mathbf{k}}^{0} \right) \mathbf{v}_{n\mathbf{k}} \otimes \mathbf{F}_{n\mathbf{k}}, \tag{4}$$

where e is the elementary charge and $N_{\mathbf{k}}$ is the total number of uniformly sampled $\mathbf{k}$ points. The summation runs over all the considered electron states denoted with a band index n and electronic wave vector $\mathbf{k}$. $f_{n\mathbf{k}}^{0}$, $\mathbf{v}_{n\mathbf{k}}$, and $\mathbf{F}_{n\mathbf{k}}$ represent the equilibrium Fermi-Dirac distribution, group velocity, and mean free displacement of electrons, respectively.

In addition to σ, the electronic thermal conductivity tensor can also be obtained as

$$\kappa_e = \frac{2}{N_{\mathbf{k}} V k_B T^2} \sum_{n\mathbf{k}} f_{n\mathbf{k}}^{0} \left(1 - f_{n\mathbf{k}}^{0} \right) (E_{n\mathbf{k}} - E_F)^2 \mathbf{v}_{n\mathbf{k}} \otimes \mathbf{F}_{n\mathbf{k}} - T\sigma S^2 \tag{5}$$

with

$$\sigma S = \frac{2e}{N_{\mathbf{k}} V k_B T^2} \sum_{n\mathbf{k}} f_{n\mathbf{k}}^{0} \left(1 - f_{n\mathbf{k}}^{0} \right) (E_{n\mathbf{k}} - E_F) \mathbf{v}_{n\mathbf{k}} \otimes \mathbf{F}_{n\mathbf{k}}, \tag{6}$$

where S refers to the Seebeck coefficient, and $E_{n\mathbf{k}}$ and E_F correspond to energies at the electronic $\{n\mathbf{k}\}$ state and at the Fermi level, respectively. Similar to the phonon case, $\mathbf{F}_{n\mathbf{k}}$ can be linearized as [13,16]

$$\mathbf{F}_{i\mathbf{k}} = \tau_{n\mathbf{k}} (\mathbf{v}_{n\mathbf{k}} + \mathbf{\Delta}_{n\mathbf{k}}), \tag{7}$$

where $\tau_{n\mathbf{k}}$ denotes the total electron lifetime of state $\{n\mathbf{k}\}$ limited by electron-phonon coupling (EPC) interactions. As in the phonon BTE, we can also solve $\mathbf{F}_{n\mathbf{k}}$ with an iterative scheme, and eventually obtain the exact σ and κ_{e} tensors (see Supplemental Material) [12].

III. COMPUTATIONAL DETAILS

The density functional theory (DFT) and density functional perturbation theory (DFPT) calculations were performed using QUANTUM-ESPRESSO code [17]. The optimized norm-conserving Vanderbilt pseudopotential and Perdew-Burke-Ernzerhof functional were employed [18,19]. For the structural optimization, we had performed the atomic-position relaxation with cell parameters fixed at the experimental values. For comparison, the variable-cell relaxation was also performed. The energy cutoff for the wave function was set to 80 Ry. Methfessel-Paxton smearing with a broadening of 0.01 Ry for occupation of electronic states and a 40×40×40 $\mathbf{k}$-grid to separate the Brillouin zone were also used. The structure was regarded as converged with the energy and force differences less than 10^{-10} Ry and 10^{-9} Ry/Bohr, respectively. The self-consistent calculations were then performed with a 20×20×20 $\mathbf{k}$-grid.

The phonon dispersion was calculated under a 5×5×5 $\mathbf{q}$-grid using DFPT, while the non-self-consistent calculations and initial EPC matrix elements were obtained with a coarse 10×10×10 $\mathbf{k}$-grid. The EPW code [20] was then adopted to execute Wannier function interpolation for the EPC matrix elements. The electronic transport properties were calculated by using our home-developed BTE solver [13,16]. After a rigorous convergence test, fine 150×150×150 $\mathbf{k}$- and $\mathbf{q}$-grids were used to obtain converged values of σ and κ_{e} above 150 K. Denser $\mathbf{k}$- and $\mathbf{q}$-grids of 350×350×350 were used at lower temperatures. σ and κ_{e} were well converged at and above 100 K, but not fully converged below 100 K. However, due to the limit of our computational resources, we cannot go beyond that dense grid. The converged phonon-electron scattering rates were calculated with a 60×60×60 $\mathbf{k}$-grid and a 30×30×30 $\mathbf{q}$-grid.

The thirdorder.py code [10], using the supercell finite-difference method, was employed to determine the third-order interatomic force constants (IFCs) with a 4×4×4 supercell and Γ only $\mathbf{q}$ sampling. We considered up to 10th nearest neighbors, which yields converged three-phonon scattering rates. Finally, the ShengBTE package [10] was modified to incorporate phonon-electron scattering to calculate κ_{ph} on a 30×30×30 $\mathbf{q}$-grid. In addition, the average squares of electronic group velocity for Sb and Bi were calculated by the above approaches for comparison [21], and the three-phonon scattering rates of Ge were calculated using the parameters in Ref. [22].

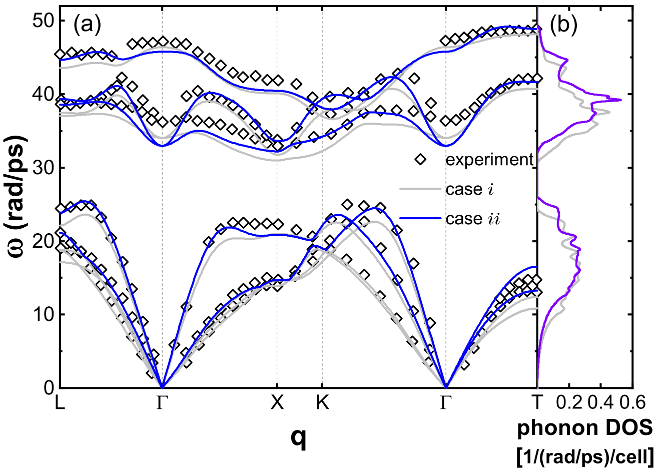

FIG. 1. (a) Calculated phonon dispersion for As using two sets of structural parameters described in the text, each with (b) phonon density of states. The hollow diamonds correspond to experimental data [23].

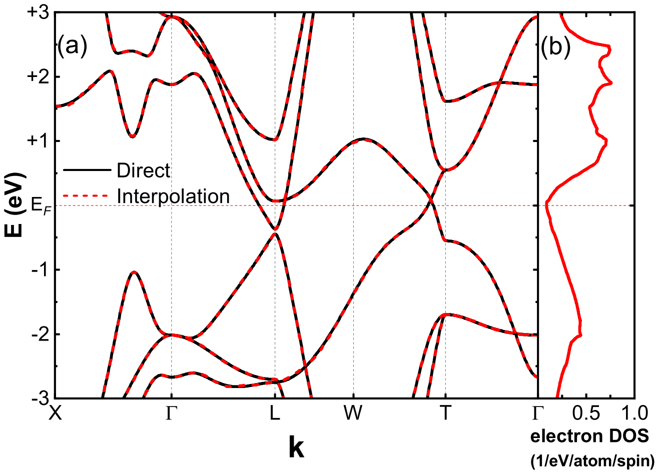

FIG. 2. (a) Calculated electronic band structures around the Fermi level with (b) electronic density of states. Black solid and red dashed lines represent the direct calculated and Wannier function interpolated results.

IV. RESULTS AND DISCUSSION

A. Phonon dispersion

Calculating thermal transport properties in metals, which arise primarily from phonon-phonon and electron-phonon interactions, requires accurate descriptions of phonon dispersion and electronic structure. The elemental arsenic, with the stable rhombohedral A7 structure, involves two atoms per primitive cell. Figure 1(a) shows the calculated and measured phonon dispersion for As along high-symmetry directions [23]. The calculated phonon-dispersion curves are obtained using two sets of cell parameters, characterized by the lattice constant (a) and rhombohedral angle (θ): (i) $a = 4.227$ Å and $\theta = 53.63^\circ$ obtained with variable-cell relaxation; (ii) $a = 4.102$ Å and $\theta = 54.55^\circ$, corresponding to the atomic-position relaxation with both a and θ fixed at the experimental values [21]. The $\sim$3% overestimation of the lattice constant in case (i) results from the well-known underbinding of PBE functional [24].

For case (i), phonon frequencies appear to be smaller as compared to the measured data, again due to the underbinding of the PBE functional. On the other hand, for case (ii), with measured a and θ, almost all the phonon frequencies reach a better agreement with the measured data except the two lowest optical branches around the Γ point. The evident phonon frequency decrease in case (i) can also be seen from the phonon density of states (DOS) in Fig. 1(b) as compared with case (ii). To better understand the practical thermal transport in As, all the quantities in the following calculations are determined by case (ii).

The phonon dispersion of As is somewhat similar to that of other group-V semimetals Bi and Sb, since they have the same A7 structure [25] and electronic configurations (e.g., same column in the Periodic Table). Therefore, the differences in phonon dispersion between As, Sb, and Bi come from the harmonic IFCs and atomic masses. Note that ω^2 directly relates to the inverse of mass and harmonic IFCs. When comparing with the calculated phonon dispersion of Sb and Bi [25], even replacing the atomic mass of As with that of Sb or Bi, As still has higher phonon frequencies than Sb and Bi (Fig. S2) [12]. This indicates that As should have a stronger harmonic component of interatomic potential than Sb and Bi. In fact, a stronger bonding strength of As than that of Sb and Bi has been revealed before [26]. Despite the similarity in the shape, some obvious differences between As, Sb, and Bi still appear. For instance, the softer TO modes at Γ than at T, which implies stronger crystal anharmonicity [27], are more evident in Sb and Bi than in As (Fig. S2) [12]. The acoustic phonons in As, especially for the LA branch, along the Γ-X-K-Γ line (in the binary plane), are obviously stiffer than along the Γ-T (trigonal direction) line. However, the acoustic phonons along various lines display less anisotropy in Sb and Bi than in As. These differences can lead to different phonon transport behaviors.

Semiconducting Ge, one neighboring element of As in the Periodic Table, stabilizes in the diamond structure, and has an atomic mass of 3% smaller than As. The phonon dispersion spans a similar range for As (up to $\sim$50 rad/ps) and Ge (up to $\sim$53 rad/ps) [22]. However, since they have different crystal structures, the phonon-dispersion features are quite distinct. The most evident difference is that an acoustic-optical phonon gap is present for As but not for Ge. In addition, there is also a stronger bunching of acoustic modes in As than in Ge.

B. Electronic band structure

Our Wannier function interpolated band structure (Fig. 2) is in excellent agreement with the direct calculation around the Fermi level (E_F), and previously calculated results [5,28]. Evidently around E_F, small electron and hole pockets appears near L and T points separately, demonstrating a narrow overlap between conduction and valence bands [5]. The electron density of states (DOS) is minimized near E_F, which is typical of semimetals. The minimized electron DOS near E_F in As is the outcome of rhombohedral A7 structure, which is slightly distorted from the metallic simple-cubic structure. The effect

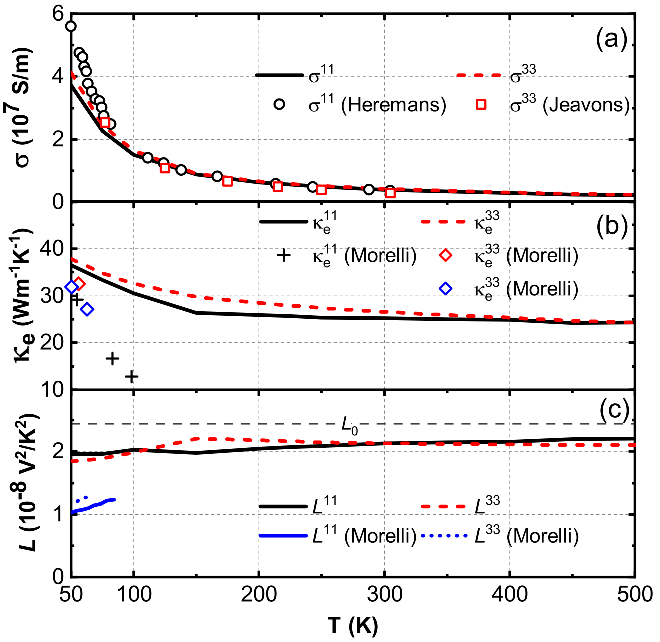

FIG. 3. Calculated (a) electronic conductivity, (b) electronic thermal conductivity, and (c) Lorenz number in binary (11) and trigonal (33) directions. Note that the results are not well converged below 100 K. The symbols show the corresponding experimental data taken from Heremans *et al.* [9], Jeavons *et al.* [34], and Morelli *et al.* [8]. The blue and red hollow diamonds are for κ_e^{33} measured from different samples.

of distortion is to open a gap around E_F, which can largely reduce the energy band crossings and degeneracy, i.e., decrease the electron DOS there [29–31].

The stability of the A7 structure in As is explained by the Peierls distortion mechanism [32]. In the covalent pictures, As has weak *sp* hybridization with *s*-band below *p*-band. Hence, the chemical bonding is made of *p*-electrons, which usually build simple-cubic structure. However, these valence *p*-bondings in As are unsaturated, failing to form stable simple-cubic structures [28,33]. Instead, the distortion serves to form short and long bonds in three almost orthogonal directions by delocalizing electrons, making the A7 structure layered [23].

C. Electronic thermal conductivity

The crystallographic binary- and trigonal-oriented σ are the diagonal components of σ tensor, which can be denoted as σ^{11} and σ^{33}, respectively. Likewise, the labels 11 and 33 are also used to specify binary and trigonal components, respectively, for other transport quantities. As shown in Fig. 3(a), the calculated σ is nearly isotropic. Below 100 K, the unconverged calculations (Fig. S5) [12] underestimate those experimental results significantly, for instance by 50% at 50 K. Above 100 K, in contrast, σ^{11} agrees well with the measured results, and σ^{33} is larger than the measured results by as much as ~40%. Specifically at 300 K, the calculated σ^{11} and σ^{33} are 3.95 and 4.16 μS/m, respectively, while they were measured to be 3.73 and 2.93 μS/m at 305 K. Typically it is not easy to measure σ^{33} precisely due to difficulties of high-quality single-crystal growth and easy crystal cleavage in this direction [8,34].

TABLE I. Comparison of $v_{F,\alpha}^2$, κ_e (300 K), and κ_{ph} (300 K) among As, Sb, and Bi in the binary (11) and trigonal (33) directions. In Sb and Bi, κ_e values are obtained by subtracting the calculated κ_{ph} [25] from the measured κ_t [36,37].

	As	Sb	Bi
$v_{F,11}^2$ $[10^4\ (\mathrm{km/s})^2]$	20.5	10.9	9.07
$v_{F,33}^2$ $[10^4\ (\mathrm{km/s})^2]$	20.8	12.7	4.73
κ_e^{11} $(\mathrm{W\,m^{-1}\,K^{-1}})$	26.6	15.2	6.3
κ_e^{33} $(\mathrm{W\,m^{-1}\,K^{-1}})$	25.2	13.2	2.9
κ_{ph}^{11} $(\mathrm{W\,m^{-1}\,K^{-1}})$	18.6	5.1	3.5
κ_{ph}^{33} $(\mathrm{W\,m^{-1}\,K^{-1}})$	5.8	6.1	3.1

The calculated κ_e is also nearly isotropic with a room-temperature value of 25.2 and 26.6 $\mathrm{W\,m^{-1}\,K^{-1}}$ in binary and trigonal directions, respectively [Fig. 3(b)]. The isotropic behavior is in line with the low-temperature measurements between 20 and 80 K [8]. κ_e is found to be almost independent of T in the range from 150 to 500 K. For instance, κ_e^{33} only decreases from 29.7 $\mathrm{W\,m^{-1}\,K^{-1}}$ at 150 K to 24.3 $\mathrm{W\,m^{-1}\,K^{-1}}$ at 500 K. The weak temperature dependence of κ_e at high temperatures is a typical characteristic of metals [35]. At 100 K, the calculated values are more than twice as large as those reported by Morelli *et al.* [8]. At 50 K, it seems that the calculations are slightly larger than the measurements. However, we expect that the converged values can be much larger (see the discussions below).

From Eqs. (4) and (5), it can be seen that only the states around the Fermi level contribute to the transport properties. Hence, the anisotropy of σ and κ_e mainly originates from the anisotropy in the square of electronic group velocity along different directions averaged at the Fermi level $v_{F,\alpha}^2$ (α denotes binary or trigonal direction). $v_{F,\alpha}^2$ for the binary and trigonal directions are almost the same with ~2% difference (Table I), resulting in an isotropy of κ_e and σ. To compare with Sb and Bi, we subtract the calculated κ_{ph} [25] from the measured κ_t [36,37]. Interestingly, as summarized in Table I, the nearly isotropic behavior of κ_e is also observed in Sb, but not in Bi, where κ_e is highly anisotropic. For Sb, the binary component of v_F^2 only differs slightly from the trigonal one, whereas Bi exhibits a roughly twofold difference in $v_{F,\alpha}^2$ values between these directions.

Our calculation of κ_e [Eq. (5)] is a full band calculation, so explicit separation of electron and hole contributions is not needed. However, one may wonder how these contributions are compared to the bipolar contribution. The bipolar component of κ_e can be obtained as $\kappa_b = T\sigma_n\sigma_p(\sigma_n+\sigma_p)^{-1}(S_p - S_n)^2$ [38], where σ_p (σ_n) and S_p (S_n) are the σ and S tensors due to holes (electrons) alone. κ_b is appreciable only when $\sigma_n \approx \sigma_p$, which can occur in semimetals [39] and doped semiconductors [40]. For As, the calculated σ_n and σ_p are found to be comparable (Fig. S7) [12], qualitatively consistent with the previous results measured from the mobility ratio [41]. In our calculations, both binary- and trigonal-oriented κ_b in As,

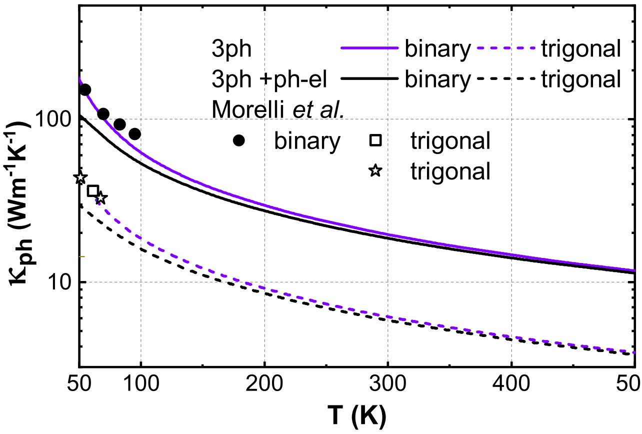

FIG. 4. The calculated lattice thermal conductivity of As in binary and trigonal directions with considering three-phonon (3ph) scattering individually and combined with phonon-electron (ph-el) scattering. The black symbols are taken from measurement [8]. The hollow square and stars indicate the trigonal-oriented κ_{ph} from different samples.

with room-temperature values of 13.4 and 15.6 W m^{-1} K^{-1}, respectively, account for more than 50% of κ_{e}, similar to the Bi case [7,42].

The Lorenz number, $L = \kappa_{\text{e}}/\sigma T$, is ideally equal to the Sommerfeld value of $L_0 = 2.44\times10^{-8}$ V^2/K^2 [1,4]. All our calculated L agree with L_0 within 23%, lying in (1.8–2.2)$\times$ 10^{-8} V^2/K^2. However, the measured L along these two directions, reported only up to 80 K, are significantly smaller, and less than 50% of L_0. The measured L are much smaller than the calculated ones due to the smaller κ_{e} extracted experimentally. Our calculations below 100 K are not fully converged, and we expect that fully converged results would lead to a reduction of L. However, it is not likely that they can reach as small as the measured L. Actually L is supposed to approach L_0 above the Bloch-Grüneisen temperature θ_{BG} [43]. Considering that semimetals such as As have short Fermi vectors, θ_{BG} of As is a few tens of Kelvin [9]. We also note that L in the binary direction also agree well with L_0 down to 60 K in Bi with a smaller θ_{BG} [7]. Therefore, κ_{e} in As needs further examinations in order to clarify the large discrepancy of measured L from L_0. κ_{e} is estimated to be 42 W m^{-1} K^{-1} based on the measured σ of 5.6×10^7 S/m assuming $L = 1.5\times10^{-8}$ V^2/K^2 at 50 K.

D. Lattice thermal conductivity

The calculated κ_{ph} along these two directions is plotted in Fig. 4. The calculated κ_{ph} underestimates the experimental values reported up to 100 K by Morelli *et al.* [8], which were obtained by subtracting κ_{e} from κ_{t}. As mentioned earlier, the experimentally reported κ_{e} were actually smaller than our calculations.

The calculated κ_{ph}^{11} and κ_{ph}^{33} are 18.6 and 5.8 W m^{-1} K^{-1} at 300 K, respectively. We want to stress that the room-temperature value of κ_{ph} in the binary direction for As is larger than those for most other elemental metals [14,44], such as Al (9.0 W m^{-1} K^{-1}) and Cu (17.4 W m^{-1} K^{-1}), with exceptions for W (46 W m^{-1} K^{-1}) [16], Mo (37 W m^{-1} K^{-1}) [11], and Ni (23 W m^{-1} K^{-1}) [45].

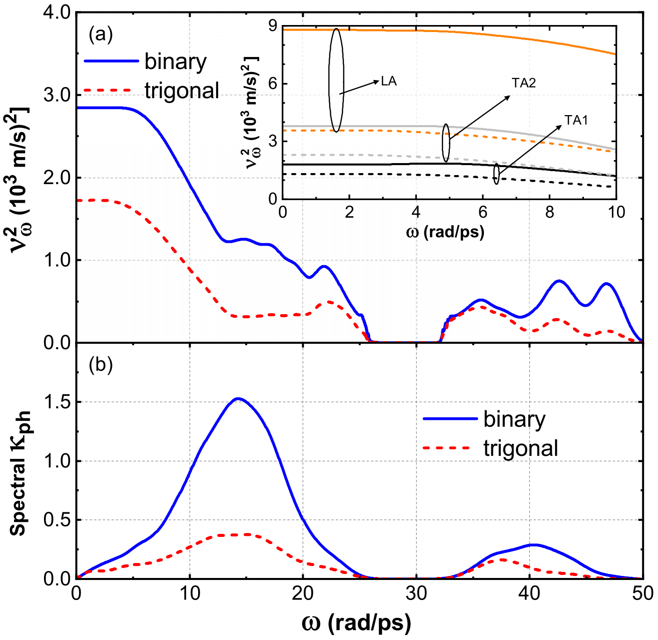

FIG. 5. (a) The averaged square of the phonon group velocity of As along binary (solid line) and trigonal (dashed line) directions. The inset shows the corresponding values of the low-frequency LA, TA1, and TA2 branches, respectively. (b) The calculated spectral contributions to κ_{ph} at 300 K in these directions.

Anisotropy of κ_{ph}. Strongly anisotropic κ_{ph} is found in As, with the ratio of $\kappa_{\text{ph}}^{11}/\kappa_{\text{ph}}^{33}$ being almost constant and ∼3.2 at 300 K. This large anisotropic factor for the binary/trigonal κ_{ph} is unusual in bulk elemental metals, but it is smaller than those in other strongly anisotropic layered systems, such as 5 to 23 for black phosphorus [46] and even 47 for graphite [47]. Experimentally, the κ_{ph} measured up to 100 K has also been revealed to display strong anisotropy, with anisotropic factors close to our calculated ones [8].

Similar to the κ_{e} case and from Eq. (1), the anisotropy of κ_{ph} mainly results from the anisotropy in the square of phonon group velocity along different directions $\text{v}_{\lambda,\alpha}^2$. However, in contrast to κ_{e}, where only states around the Fermi level are relevant, phonon modes within a wide frequency range can contribute to κ_{ph} effectively. Hence, to understand the anisotropy of κ_{ph}, we define $\text{v}_{\omega,\alpha}^2 = \sum_\lambda \text{v}_{\lambda,\alpha}^2 \delta(\omega - \omega_\lambda)/\sum_\lambda \delta(\omega - \omega_\lambda)$, corresponding to the average of $\text{v}_{\lambda,\alpha}^2$ over phonon modes with the same frequency ω. Figure 5(a) shows the $\text{v}_{\omega,\alpha}^2$ along the binary and trigonal directions dependent on ω at 300 K. We can observe that the $\text{v}_{\omega,\alpha}^2$ for the trigonal direction is dramatically lower than those for the binary direction, particularly for the acoustic ω range. Note that the phonons within the acoustic ω range make the predominant contribution to κ_{ph}. To be quantitative, the frequency-contributed κ_{ph} curves along these directions are also plotted in Fig. 5(b). Acoustic phonons (below 25 rad/ps) contribute 87% and 82% to κ_{ph} along these directions, respectively. Therefore, the obvious discrepancy of low-frequency $v_{\omega,\alpha}^2$ in binary and trigonal directions mainly accounts for the anisotropy of κ_{ph}. To

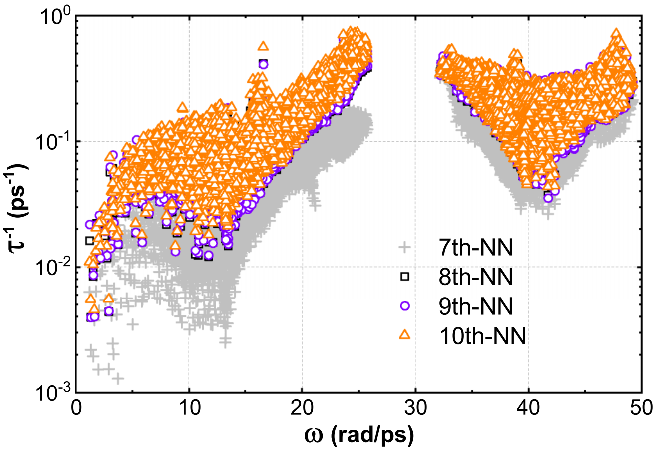

FIG. 6. The comparison of three-phonon scattering rates with third-order interatomic force constants considering up to different nearest neighbors (NN).

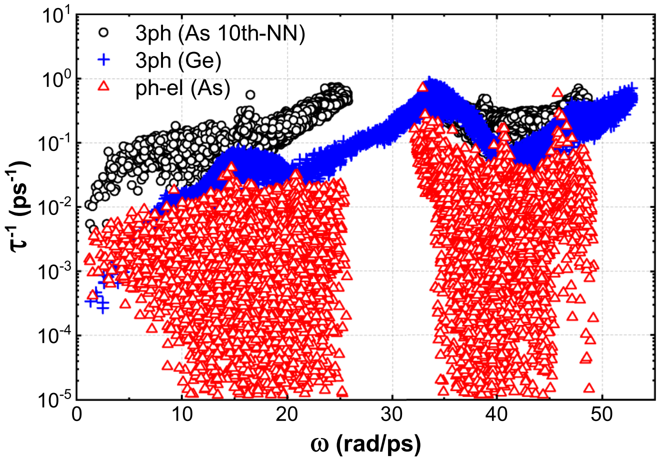

FIG. 7. Comparison of the three-phonon and phonon-electron scattering rates of As and three-phonon scattering rates of Ge.

further see which phonon branch induces the acoustic anisotropy, we compare $v^2_{\omega,\alpha}$ values of three acoustic phonon branches at low-ω as plotted in the inset of Fig. 5(a). At low frequencies, there is a significant difference in $v^2_{\omega,\alpha}$ for the LA branch in these directions, which can help explain the strong anisotropy in As κ_{ph}.

As shown in Sec. IV C, As and Sb have almost isotropic κ_{e}, whereas Bi has a twofold anisotropy. The anisotropic behaviors of κ_{ph} in these three semimetals are different from those of κ_{e}. As revealed in previous calculations (Table I) [25], κ_{ph} can be regarded as isotropic in Sb and Bi, as compared to the more than threefold anisotropy in As. To some extent, the isotropy of κ_{ph} in Sb and Bi or the anisotropy in As can be understood as a consequence of different phonon-dispersion features, as discussed in Sec. IV A. Nevertheless, these distinctions show that small distortion of the structure with a different extent can have a prominent effect on the transport properties.

Three-phonon scattering effect. Any phonon scattering process can contribute to the κ_{ph} reduction. For isotopically pure As, only the three-phonon and phonon-electron scatterings can have effects on κ_{ph}. We first explore the three-phonon scattering rates at 300 K (Fig. 6). Most phonons have comparable scattering strength in the three-phonon process, with scattering rates ranging from 0.01 to 1 ps^{-1}, largely limiting κ_{ph}.

It was found in previous works that Sb and Bi have strong crystal anharmonicity, leading to low κ_{ph} [25,27]. It is traced by the non-negligible third-order IFCs at long-range interactions. Fundamentally, these non-negligible anharmonic interactions stem from the resonant interatomic bonding, which makes valence p-electrons delocalized in forming stable chemical bonds under the distorted A7 structure, and they can greatly affect long-range harmonic and anharmonic interactions. For isostructural As, the resonant bonding effect on long-range interactions should also be applied. In fact, the unusual bonding has been observed in As, characterized by the enlarged harmonic interactions with the eighth nearest neighbors [23]. In our work, we have also found that the third-order anharmonic interactions enlarge at the eighth nearest neighbors (NN).

To quantitatively reveal this enhanced anharmonicity effect on scattering at the mode-specific level, we plot three-phonon scattering rates obtained with third-order IFCs up to the seventh through tenth NN interactions in Fig. 6. An overall (about threefold) increase in the phonon scattering rates occurs when considering the anharmonic IFCs at the eighth NN interaction, particularly for the acoustic regions of 0–13 rad/ps. As revealed in Fig. S1 [12], κ_{ph} is mainly limited by two types of scattering channels: three acoustic phonons (*aaa*), and two acoustic and one optical phonons (*aao*).

κ_{ph} of As is much smaller than that for isotopically pure Ge (54 W m^{-1} K^{-1}) [22]. This is because As has much larger anharmonic scattering rates in the acoustic region (Fig. 7). Actually, the phonon dispersion suggests that As has weaker scattering phase space than Ge. The acoustic-optical gap in As restricts the *aao* channels, and more bunching among acoustic modes in As impedes the *aaa* processes. Therefore, the stronger anharmonic scattering in As is indicative of stronger anharmonicity in the interatomic potential.

Phonon-electron scattering effect. At 300 K and above, the κ_{ph} calculated without including the phonon-electron scattering is larger than the actual κ_{ph} by less than 5% for both directions. At lower temperatures, the three-phonon scattering becomes weaker, and the phonon-electron scattering remains unchanged. As a result, phonon-electron scattering can affect the κ_{ph} at lower temperatures. For example, at 50 K, after excluding the phonon-electron scattering, κ_{ph} increases by 30%.

The phonon-electron scattering rates at 300 K are also shown in Fig. 7. The phonon-electron scattering rates are generally more than one order of magnitude lower than those for three-phonon scattering at 300 K, which explains the negligible effect of phonon-electron scattering on κ_{ph} at room and high temperatures. On the other hand, the phonon-electron scattering rates are quite dispersed, quite in contrast to those for three-phonon scattering. The phonon-electron scattering rates do not follow a simple ω dependence at low frequencies, which is also distinct from the linear ω dependence in other metals [11,16,48]. The dispersed rates are characteristic of semimetals and heavily doped semiconductors with

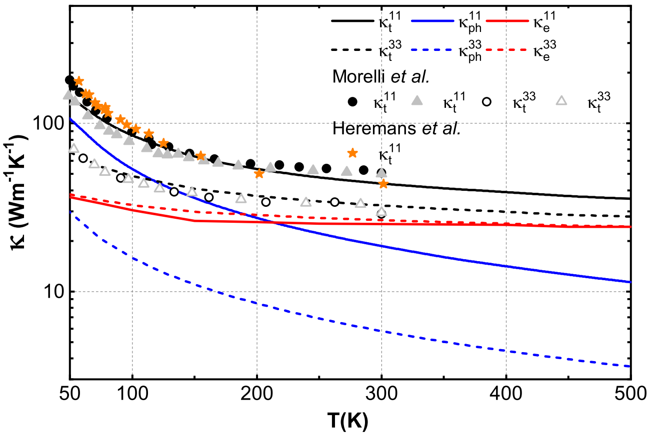

FIG. 8. The calculated total thermal conductivity of As in binary (11) and trigonal (33) directions, together with the individual phonon and electronic contributions. Note that the results are not fully converged below 100 K. The symbols represent the measured total thermal conductivity taken from Heremans *et al.* [9] and Morelli *et al.* [8].

a small Fermi surface [49,50]. When the Fermi surface is small and composed of separated pockets [51], the scattering rates depending on the number of scattering channels become extremely sensitive to the specific phonon mode. When the phonon wave vectors cannot connect two different electronic states at the Fermi surface, the scattering of those phonon modes by electrons cannot happen. Furthermore, considering that low-frequency phonon-electron scattering rates are positively correlated with the carrier density [49,50], the elemental Bi and Sb, with lower carrier densities, are expected to exhibit weaker phonon-electron scattering, which should have a negligible effect on κ_{ph}.

E. Total thermal conductivity

Our calculated total thermal conductivity κ_{t}^{11} and κ_{t}^{33} agree well with the experimental data, as shown in Fig. 8. Below 100 K, the calculated κ_{t}^{11} and κ_{t}^{33} underestimate the measured values slightly, mainly because the calculated κ_{e} is not fully converged. At room temperature, the calculated κ_{t}^{11} and κ_{t}^{33} in As reach 43 and 32 W m^{-1} K^{-1}, respectively. However, as mentioned earlier, the calculated individual contributions κ_{e} and κ_{ph} deviate from those reported experimental values. Considering the good agreement for the total thermal conductivity, we suggest that this discrepancy for individual contributions may result from the experimental challenge in separating κ_{e} and κ_{ph}.

To make the separation, Morelli *et al.* measured the thermal conductivity as a function of transverse magnetic field. When thermal conductivity gets saturated, κ_{e} is completely suppressed. The final saturated value corresponds to κ_{ph}. Due to the limit of magnetic field, the thermal conductivity can saturate only up to 37 K for As. For higher temperatures, κ_{e} was first estimated from an extrapolation method, and then subtracted from κ_{t} to obtain the reported κ_{ph} up to 100 K [8]. However, the extrapolation method employed usually has limited accuracy at high temperatures [52]. Moreover, assuming κ_{e} can be completely suppressed by a large transverse magnetic field also needs careful verification. In fact, when applying a strong enough magnetic field, the first term in Eq. (5) for κ_{e} can indeed be eliminated. However, there remains a second term related to the Seebeck coefficient, which does not necessarily vanish [7,53]. Due to a large thermomagnetic response [54,55], κ_{e} can be nonvanishing, and thus the separation requires a detailed analysis, particularly in semimetals. Actually a field-dependent thermomagnetic power of As was observed to undergo obvious oscillations at low temperatures [56]. Likely for Bi, there remains a significant electronic contribution from the transverse thermomagnetic effects even in the high magnetic field limit [7].

In Sb and Bi, by comparing the calculated κ_{ph} and measured κ_{t}, it was found that electrons and phonons have comparable contributions to the thermal conductivity [25], except at very low temperatures where the κ_{ph} predominates. Our calculations show that As has similar features, especially for the binary direction. At 300 K, the binary-oriented κ_{e}^{11} is ∼57% of κ_{t}^{11}, while the trigonal-oriented κ_{e}^{33} contributes predominantly (80%) to κ_{t}^{33}. These electronic contributions in both directions decrease at lower T. Below 200 K, κ_{ph} starts to dominate over κ_{e} in the binary direction, whereas in the trigonal direction the lattice contribution becomes governable when T falls beneath 50 K. We note that when T goes down further (10 K, for instance) in As, the experiments suggest κ_{ph} should become negligible as compared to κ_{e}, due to large phonon-electron scattering [8]. This is in contrast to Sb and Bi, where κ_{ph} only dominates over κ_{e} at very low temperatures.

V. CONCLUSION

We have quantified the electronic and lattice contributions to total thermal conductivity of arsenic between 50 and 500 K with the framework of BTE from first principles. The thermal transport properties of As exhibit different characteristics from Sb and Bi. The calculated κ_{e} is nearly isotropic, and almost temperature-independent above 150 K with a room-temperature value of 25.2 and 26.6 W m^{-1} K^{-1} along binary and trigonal directions, respectively. However, κ_{ph} is highly anisotropic, mainly due to the anisotropic acoustic phonons, especially for the LA branch. The calculated room temperature κ_{ph} are 18.6 and 5.8 W m^{-1} K^{-1}, contributing 43% and 20% to the total thermal conductivity along the binary and trigonal directions, respectively. κ_{ph} along the binary direction is larger than those for most of the other elemental metals, and becomes predominant over κ_{e} below 200 K. We also find that the harmonic interatomic interactions in As are comparable to those in Ge, while the anharmonic interactions are stronger in As. In addition, the phonon-electron scattering, nearly one order of magnitude weaker than three-phonon processes, hardly affects κ_{ph} at room temperature. The calculated κ_{t} in both directions and electrical conductivity in the binary direction agree well with the measured values, which suggests that previous experimental separation of κ_{ph} and κ_{e} is likely inaccurate. Lastly, the calculated electrical conductivity along the trigonal direction is larger than the measured value by about 40%. This discrepancy deserves further study, both experimentally and theoretically.

ACKNOWLEDGMENTS

We acknowledge support from the Natural Science Foundation of China (NSFC) (Grants No. 12174261 and No. 12104312), the Stable Support Plan of the Higher Education Institutions of Shenzhen (Grant No. 20200809161605001), and the GuangDong Basic and Applied Basic Research Foundation (Grants No. 2021A1515010042, No. 2022A1515011877, and No. 2023A1515010365).

---

[1] J. Ziman and P. W. Levy, Phys. Today **14**(11), 64 (1961).
[2] R. Peierls and R. E. Peierls, *Quantum Theory of Solids* (Oxford University Press, Oxford, UK, 1955).
[3] R. E. B. Makinson, Math. Proc. Cambridge Philos. Soc. **34**, 474 (1938).
[4] P. Klemens and R. Williams, Int. Met. Rev. **31**, 197 (1986).
[5] J. Issi, Aust. J. Phys. **32**, 585 (1979).
[6] H. M. Rosenberg, Philos. Trans. R. Soc. London Ser. Math. Phys. Sci. **247**, 441 (1955).
[7] C. Uher and H. Goldsmid, Phys. Status Solidi B **65**, 765 (1974).
[8] D. T. Morelli and C. Uher, Phys. Rev. B **28**, 4242 (1983).
[9] J. Heremans, J. Issi, A. Rashid, and G. Saunders, J. Phys. C **10**, 4511 (1977).
[10] W. Li, J. Carrete, N. A. Katcho, and N. Mingo, Comput. Phys. Commun. **185**, 1747 (2014).
[11] S. Wen, J. Ma, A. Kundu, and W. Li, Phys. Rev. B **102**, 064303 (2020).
[12] See Supplemental Material at http://link.aps.org/supplemental/10.1103/PhysRevB.108.054303 for more details on the methodology of the phonon and electron BTEs and convergence test for σ and κ_e with respect to sampling grids. The phonon dispersion comparison with Sb and Bi, various three-phonon scattering channels in As, the calculated Seebeck coefficient compared with experiments, and the bipolar thermal conductivity are also included, with Refs. [57–60] therein.
[13] W. Li, Phys. Rev. B **92**, 075405 (2015).
[14] Z. Tong, S. Li, X. Ruan, and H. Bao, Phys. Rev. B **100**, 144306 (2019).
[15] G. K. H. Madsen and D. J. Singh, Comput. Phys. Commun. **175**, 67 (2006).
[16] Y. Chen, J. Ma, and W. Li, Phys. Rev. B **99**, 020305(R) (2019).
[17] P. Giannozzi, S. Baroni, N. Bonini, M. Calandra, R. Car, C. Cavazzoni, D. Ceresoli, G. L. Chiarotti, M. Cococcioni, I. Dabo *et al.*, J. Phys.: Condens. Matter **21**, 395502 (2009).
[18] D. R. Hamann, Phys. Rev. B **88**, 085117 (2013).
[19] M. Schlipf and F. Gygi, Comput. Phys. Commun. **196**, 36 (2015).
[20] S. Poncé, E. R. Margine, C. Verdi, and F. Giustino, Comput. Phys. Commun. **209**, 116 (2016).
[21] D. Schiferl and C. Barrett, J. Appl. Cryst. **2**, 30 (1969).
[22] G. Guo, X. Yang, J. Carrete, and W. Li, J. Phys.: Condens. Matter **33**, 285702 (2021).
[23] S. Shang, Y. Wang, H. Zhang, and Z. K. Liu, Phys. Rev. B **76**, 052301 (2007).
[24] G. I. Csonka, J. P. Perdew, A. Ruzsinszky, P. H. T. Philipsen, S. Lebegue, J. Paier, O. A. Vydrov, and J. G. Angyan, Phys. Rev. B **79**, 155107 (2009).
[25] S. Lee, K. Esfarjani, J. Mendoza, M. S. Dresselhaus, and G. Chen, Phys. Rev. B **89**, 085206 (2014).
[26] X. Gonze, J. P. Michenaud, and J. P. Vigneron, Phys. Rev. B **41**, 11827 (1990).
[27] S. Lee, K. Esfarjani, T. Luo, J. Zhou, Z. Tian, and G. Chen, Nat. Commun. **5**, 3525 (2014).
[28] L. F. Mattheiss, D. R. Hamann, and W. Weber, Phys. Rev. B **34**, 2190 (1986).
[29] M. H. Cohen, L. M. Falicov, and S. Golin, IBM J. Res. Dev. **8**, 215 (1964).
[30] R. J. Needs, R. R. M. Martin, and O. H. Nielsen, Phys. Rev. B **33**, 3778 (1986).
[31] U. Argaman, D. Kartoon, and G. Makov, J. Phys.: Condens. Matter **31**, 465501 (2019).
[32] R. Bellissent, C. Bergman, R. Ceolin, and J. P. Gaspard, Phys. Rev. Lett. **59**, 661 (1987).
[33] P. Littlewood, J. Phys. C **13**, 4855 (1980).
[34] A. P. Jeavons and G. Saunders, Proc. R. Soc. London Math. Phys. Sci. **310**, 415 (1969).
[35] R. Bauer, A. Schmid, P. Pavone, and D. Strauch, Phys. Rev. B **57**, 11276 (1998).
[36] W. Yim and A. Amith, Solid-State Electron. **15**, 1141 (1972).
[37] C. Gallo, B. Chandrasekhar, and P. H. Sutter, J. Appl. Phys. **34**, 144 (1963).
[38] H. J. Goldsmid, Proc. Phys. Soc. B **69**, 203 (1956).
[39] C. Gallo, R. Miller, P. Sutter, and R. Ure Jr., J. Appl. Phys. **33**, 3144 (1962).
[40] S. Wang, J. Yang, T. Toll, J. Yang, W. Zhang, and X. Tang, Sci. Rep. **5**, 10136 (2015).
[41] A. Jeavons and G. Saunders, Solid State Commun. **8**, 995 (1970).
[42] A. L. Moore, M. T. Pettes, F. Zhou, and L. Shi, J. Appl. Phys. **106**, 034310 (2009).
[43] D. K. Efetov and P. Kim, Phys. Rev. Lett. **105**, 256805 (2010).
[44] A. Jain and A. J. H. McGaughey, Phys. Rev. B **93**, 081206(R) (2016).
[45] Y. Wang, Z. Lu, and X. Ruan, J. Appl. Phys. **119**, 225109 (2016).
[46] J. Zhu, H. Park, J. Chen, X. Gu, H. Zhang, S. Karthikeyan, N. Wendel, S. A. Campbell, M. Dawber, X. Du *et al.*, Adv. Electron. Mater. **2**, 1600040 (2016).
[47] G. A. Slack, Phys. Rev. **127**, 694 (1962).
[48] A. Kundu, J. Ma, J. Carrete, G. K. H. Madsen, and W. Li, Mater. Today Phys. **13**, 100214 (2020).
[49] B. Liao, B. Qiu, J. Zhou, S. Huberman, K. Esfarjani, and G. Chen, Phys. Rev. Lett. **114**, 115901 (2015).
[50] B. Dongre, J. Carrete, S. Wen, J. Ma, W. Li, N. Mingo, and G. K. H. Madsen, J. Mater. Chem. A **8**, 1273 (2020).
[51] P. K. Silas, P. D. Haynes, and J. R. Yates, Phys. Rev. B **88**, 134103 (2013) .
[52] J. Pernicone and P. Schroeder, Phys. Rev. B **11**, 588 (1975).
[53] I. Y. Korenblit, M. Kuznetsov, V. Muzhdaba, and S. Shalyt, Sov. Phys. JETP **30**, 1009 (1970).

[54] I. Y. Korenblit, M. Kuznetsov, and S. Shalyt, Sov. Phys. JETP **29**, 4 (1969).
[55] C. Fu, S. N. Guin, S. J. Watzman, G. Li, E. Liu, N. Kumar, V. S, W. Schnelle, G. Auffermann, C. Shekhar *et al.*, Energy Environ. Sci. **11**, 2813 (2018).
[56] F. Muntyanu, Phys. Status Solidi B **136**, 749 (1986).
[57] G. Saunders, C. Miziumski, G. Cooper, and A. Lawson, J. Phys. Chem. Solids **26**, 1299 (1965).
[58] S.-I. Tamura, Phys. Rev. B **27**, 858 (1983).
[59] J. Ma, W. Li, and X. Luo, Phys. Rev. B **90**, 035203 (2014).
[60] F. Meng, J. Ma, J. He, and W. Li, Phys. Rev. B **99**, 045201 (2019).

Correction: A grant number in the Acknowledgments contained an error and has been fixed.